Chapter 7

Acceptances and Efficiencies

The central calorimeter performance is presented before the acceptances and efficiencies are discussed. The position and energy resolutions are necessary for a Monte Carlo simulation of the different reactions which is used to determine the acceptances. The Monte Carlo is also dependent upon the angular distributions of the reactions. The trigger and analysis efficiencies are measured by reactions and presented below. The final efficiencies are tabulated for the reactions. A discussion of uncertainties of the luminosity and beam energy measurements is given at the end of this chapter.

7.1 Central Calorimeter Performance

The central calorimeter performance can be described in terms of the two algorithms outlined in the last chapter: clusterization and the pile-up determination. The resolutions for the position (θ and ϕ) and energy of a cluster are important for identification of events by kinematical fitting. Resolving the photons from symmetric

π^o decays is another important goal of the clustering algorithm. The pile-up algorithm allows for central calorimeter signals from interactions other than the trigger interaction to be identified and discarded.

7.1.1 Clustering Algorithm

The position and energy resolution of isolated clusters is determined from analysis of $J/\psi \rightarrow e^+e^-$. The positions determined from the central calorimeter (θ_{CCAL} and ϕ_{CCAL}) are compared to angles determined by the charged tracking ($\theta_{Tracking}$ and $\phi_{Tracking}$). The difference between the two position determinations is shown in figure 7.1 for *good* charged tracks, i.e. those for which all of the charged tracking components of the detector contribute to the angle determinations. The charged tracking resolutions for both angles[1] are 2.5 mrad; when unfolded from the measured differences, result in average central calorimeter angular resolutions of $\overline{\sigma_\theta} = 5.7$ mrad and $\overline{\sigma_\phi} = 12.3$ mrad. These angular resolutions result in nearly the same position distance resolutions at the counters:

$$\sigma_\theta = \frac{\sigma_{X_R}}{r}, \tag{7.1}$$

$$\sigma_\phi = \frac{\sigma_{X_W}}{r\sin\theta}, \tag{7.2}$$

$$\tag{7.3}$$

where σ_{X_R} and σ_{X_W} are the ring and wedge position resolutions, respectively, at the lead glass blocks. Both σ_{X_R} and σ_{X_W} are < 1 cm.

[1]The average angular charged tracking resolutions are 7 and 4 mrad for $\overline{\sigma_\theta}$ and $\overline{\sigma_\phi}$, respectively.

a)

b)

Figure 7.1: The central calorimeter angular resolutions (a) θ and (b) ϕ. Unfolding the charged tracking resolutions (2.5 mrad for good charged tracks), the average central calorimeter angular resolutions are $\overline{\sigma_\theta} = 5.7$ mrad and $\overline{\sigma_\phi} = 12.3$ mrad.

a)

b)

Figure 7.2: The central calorimeter energy resolution for (a) the energy range 1.5 to 4.5 GeV (e^+e^- energy deposits from J/ψ decays) and (b) the crack correction, C_c, $\times$ E_{seen}.

The e^+e^- energy deposits from J/ψ decays are between 1.5 and 4.5 GeV. Figure 7.2a shows the difference between the energy measured E_{CCAL}, including corrections for the loss due to the septa, and the predicted energy. The predicted energy is calculated from kinematics and the angles determined from the charge tracking. The contribution of the crack correction (equation 6.2),

$$C_c = \frac{E_{corr} - E_{seen}}{E_{seen}}, \tag{7.4}$$

to the energy resolution is shown in figure 7.2b where the average energy of the electrons is 2.5 GeV. A fit to figure 7.2b leads to the parameterization of the energy resolution:

$$\frac{\sigma_E}{E} = \frac{5.5\%}{\sqrt{E}} + 0.14C_c + \frac{0.005}{E}, \tag{7.5}$$

where both σ_E and E are in GeV; the last term is for pedestal fluctuations.

The response of the central calorimeter to electromagnetic showers induced by low energy gamma rays can be different from the higher energy deposits that have been used to tune the clustering algorithm. A possible non-linearity of energy scale of the counters has been a concern since the early beam energy tests, section 4.2.2. It appeared that for a 100 MeV particle, counters calibrated by particles of energy greater than 1 GeV would underestimate the energy by $\approx 10\%$. The Monte Carlo simulation of a single counter (section 4.1.1 and Appendix C) also shows this response. Figure 7.3 shows the ratio of the expected number of photoelectrons, based upon the assumption of a linear response between zero and a high energy calibration point, and the number of photoelectrons from the Monte Carlo simulation, see equation C.1 and discussion. The energy is underestimated by 10% for incident energies of 30, 50

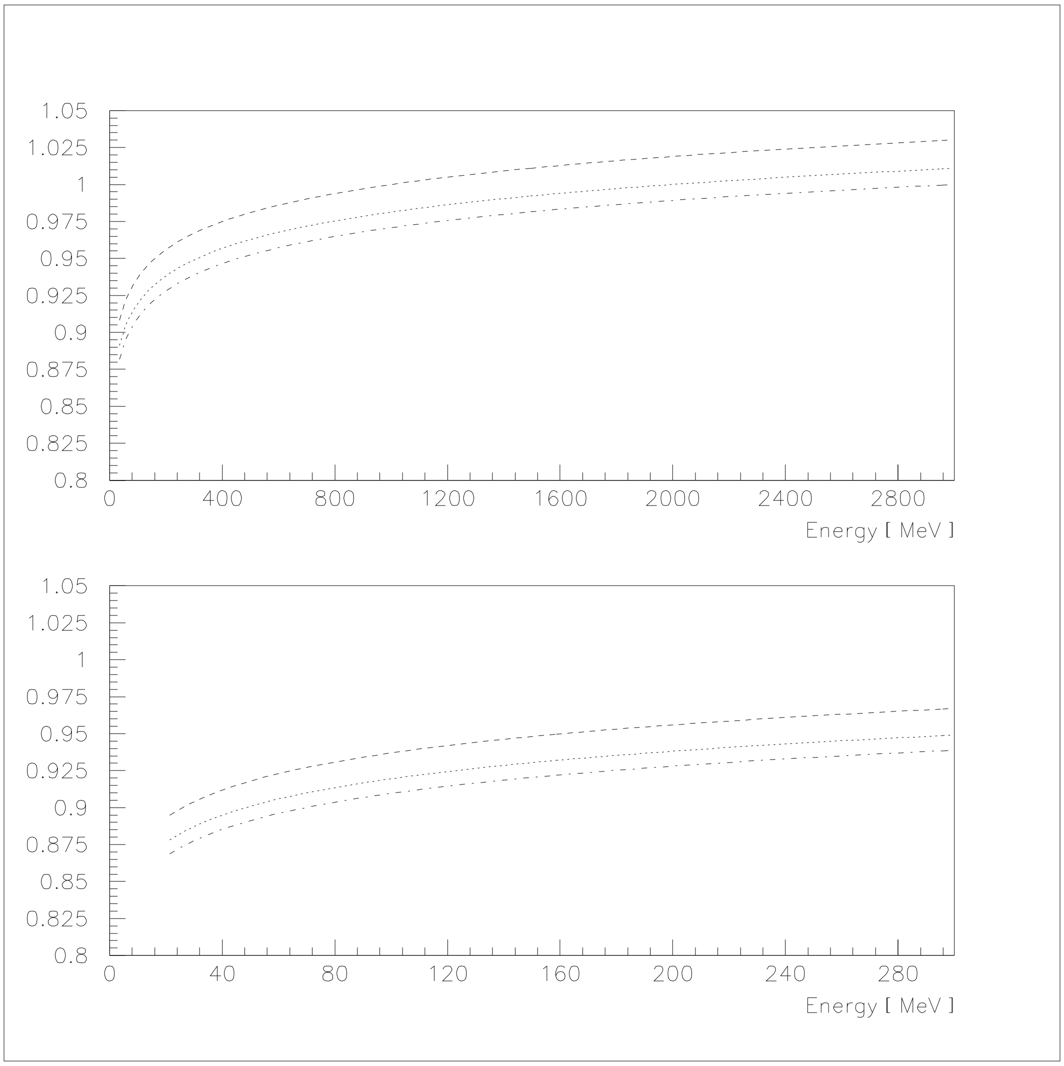

Figure 7.3: The Monte Carlo ratios of photoelectrons: linear relationship using a calibration at 1, 2, and 3 GeV (dashed, dotted, and dash-dotted, respectively) versus Monte Carlo output.

and 70 MeV when using a calibration point of 1, 2 and 3 GeV, respectively, according to this Monte Carlo prediction.

The response to low energy photons by the entire central calorimeter is better than initial indications cited above. The radiative decays of the χ_1 and χ_2 provide not only high energy e^+e^- deposits but also gamma rays of known energy as a function of polar angle, 300 MeV to 1.3 GeV. The measured energies of the photons show less

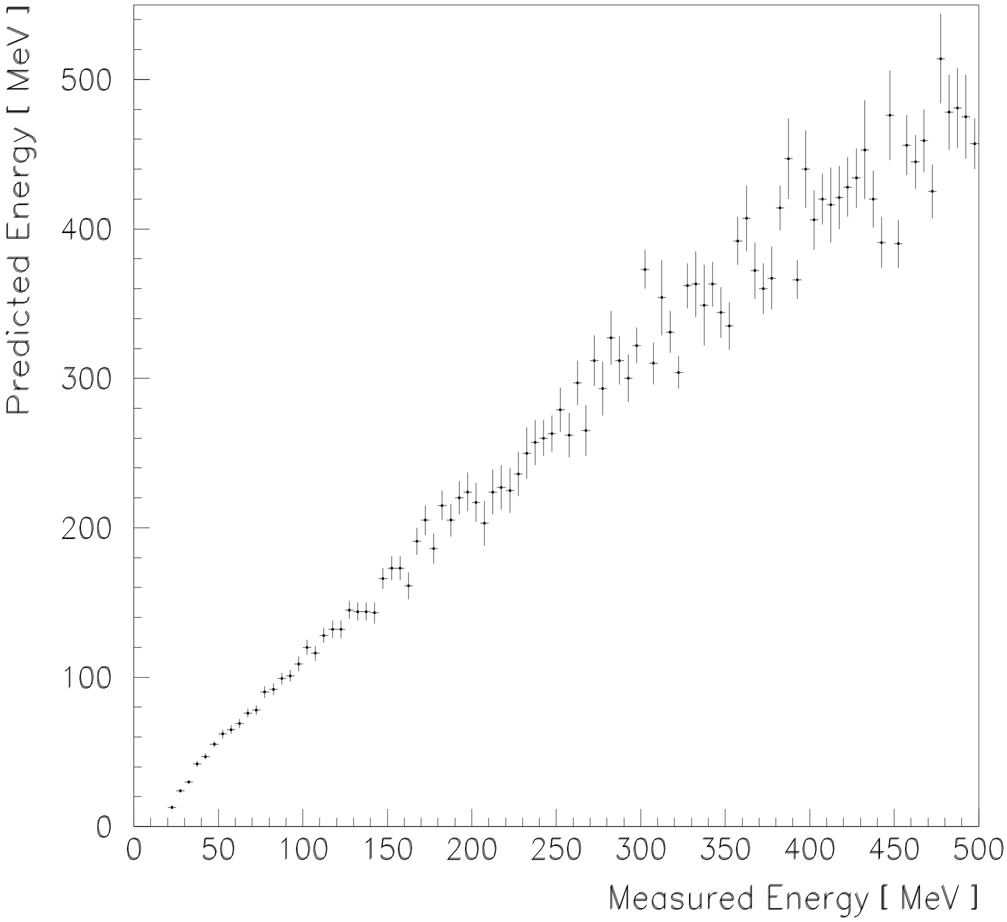

Figure 7.4: Predicted versus measured energy for the smallest energy photon from $\bar{p}p \rightarrow \pi^o\pi^o$.

than a 1% systematic shift from the predicted energies. For energy deposits less than 300 MeV, predicted energies from a $2C$ fit of $\bar{p}p \rightarrow \pi^o\pi^o$ events, where the energy of the lowest energy photon is not provided, are compared to the measured energies of the low energy photon. Figure 7.4 shows the predicted and measured energies for photon energies less than 500 MeV (perfect energy determination would result in a slope of 1.0); the average underestimation is 6%, which is comparable to the energy resolution in this energy range.

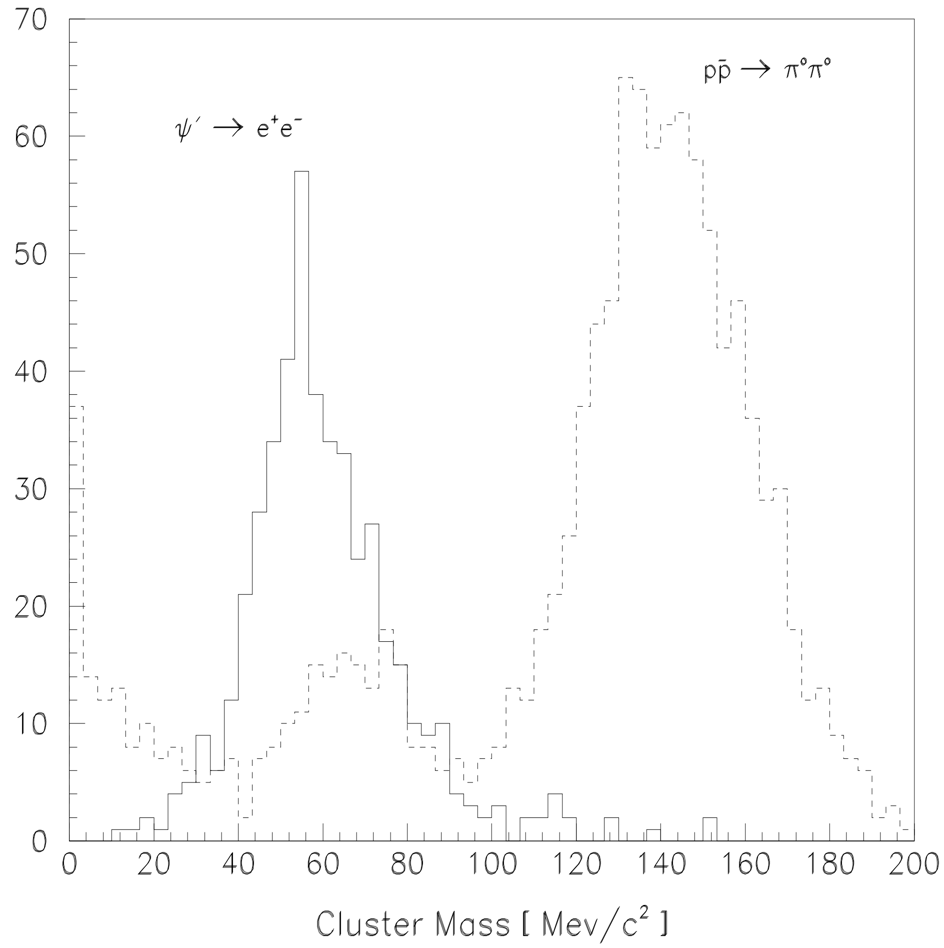

Figure 7.5: The cluster masses from exclusive e^+e^- and $\pi^o\pi^o$ events at the ψ' resonance.

The ability to separate symmetric π^o decays from isolated showers is dependent upon the cluster mass, equation 6.3. Plotted in figure 7.5 is the cluster masses for energy deposits from exclusive e^+e^- and $\pi^o\pi^o$ events from data at the ψ' resonance. The isolated showers from e^+e^- events show a peak centered near 50 MeV/c^2 with very few cluster masses > 100 MeV/c^2. The $\pi^o\pi^o$ events show three peaks: the largest peak is centered at the π^o mass and corresponds to symmetric decays where the two gamma rays are close together and are contained within a 5×5 grid; the other

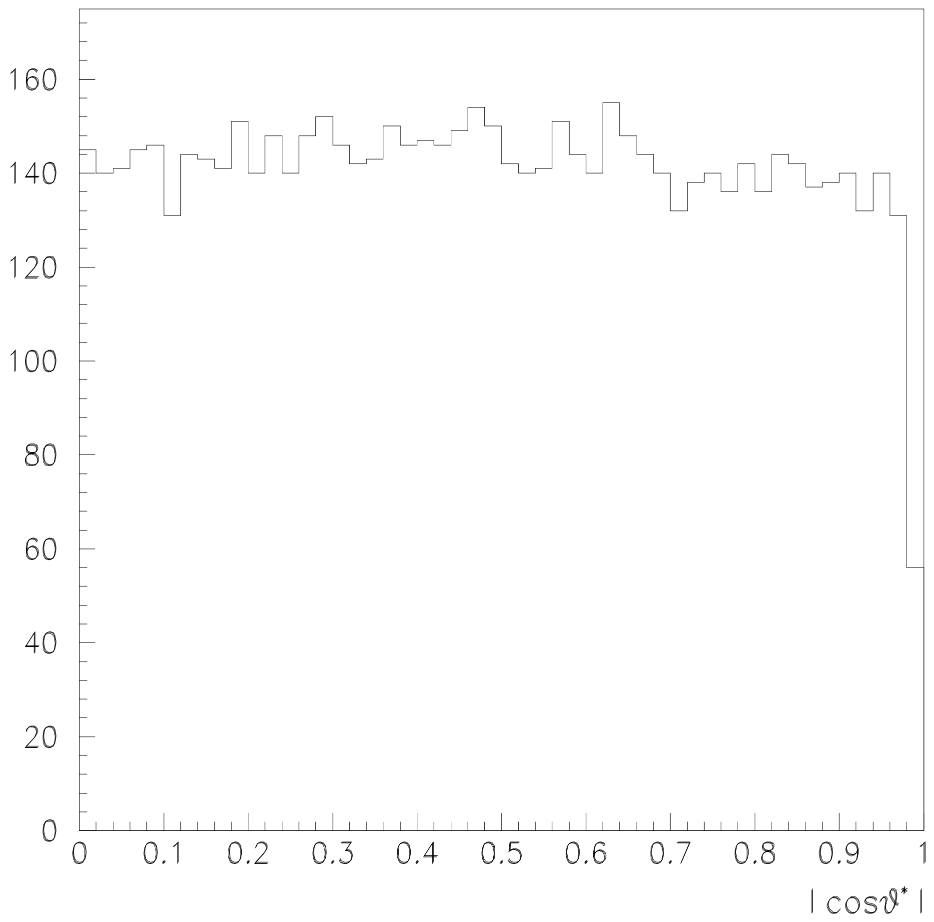

Figure 7.6: The angular distribution of photons in the π^o rest frame from $\bar{p}p \rightarrow \pi^o\pi^o$ events; θ^* is the angle between a photon's direction and the π^o boost direction. Data is for π^o's away from the central calorimeter edges.

peaks are isolated photon clusters from asymmetric decays with the lower cluster mass values coming from low energy gamma ray showers which produce signals in a small number of blocks (a single counter response results in 0 cluster mass). The ability to separate symmetric π^o decay photons and reconstruct π^o's, is shown in figure 7.6 for $15° < \theta_{\pi^o} < 50°$ in the lab, away from the central calorimeter edges. Plotted is the cosine of the angle, in the π^o rest frame, of the photon direction with respect to the

π^o boost direction, $\cos\theta^*$. The only loss in the angular distribution of photons from energetic π^o decays is from highly asymmetric π^o decays, $|\cos\theta^*| \approx 1$, where the low energy photon escapes detection.

7.1.2 Pile-up

The general philosophy of the pile-up determination was to try to avoid mislabelling signals from the triggered interaction as out-time. In trying to guarantee the correct determination of signals from the trigger interaction, signals from other interactions (which should be declared as out-time) are occasionally declared as in-time or non-determined. A set of good $\bar{p}p \rightarrow \pi^o\pi^o$ events is used to investigate the performance of the pile-up determination. This sample is selected with the following criteria: three of the four photons must have energies greater than 200 MeV; there can be no more than four clusters with energy greater than 200 MeV in the recorded event; and a four cluster $6C$ fit must have a χ^2 fit probability greater than 10%.

For large energy clusters, the pile-up routines are essentially 100% efficient for determining a signal as in-time (seen for e^+e^- decays of the J/ψ and the radiative photon from the χ states). The $\pi^o\pi^o$ events allow study down to the energy threshold of the central calorimeter. Figure 7.7 shows the efficiency of determining an interaction signal as not being out-time (i.e., either in-time or non-determined). The pile-up algorithm appears to be nearly perfect for clusters above 120 MeV. Below this cluster

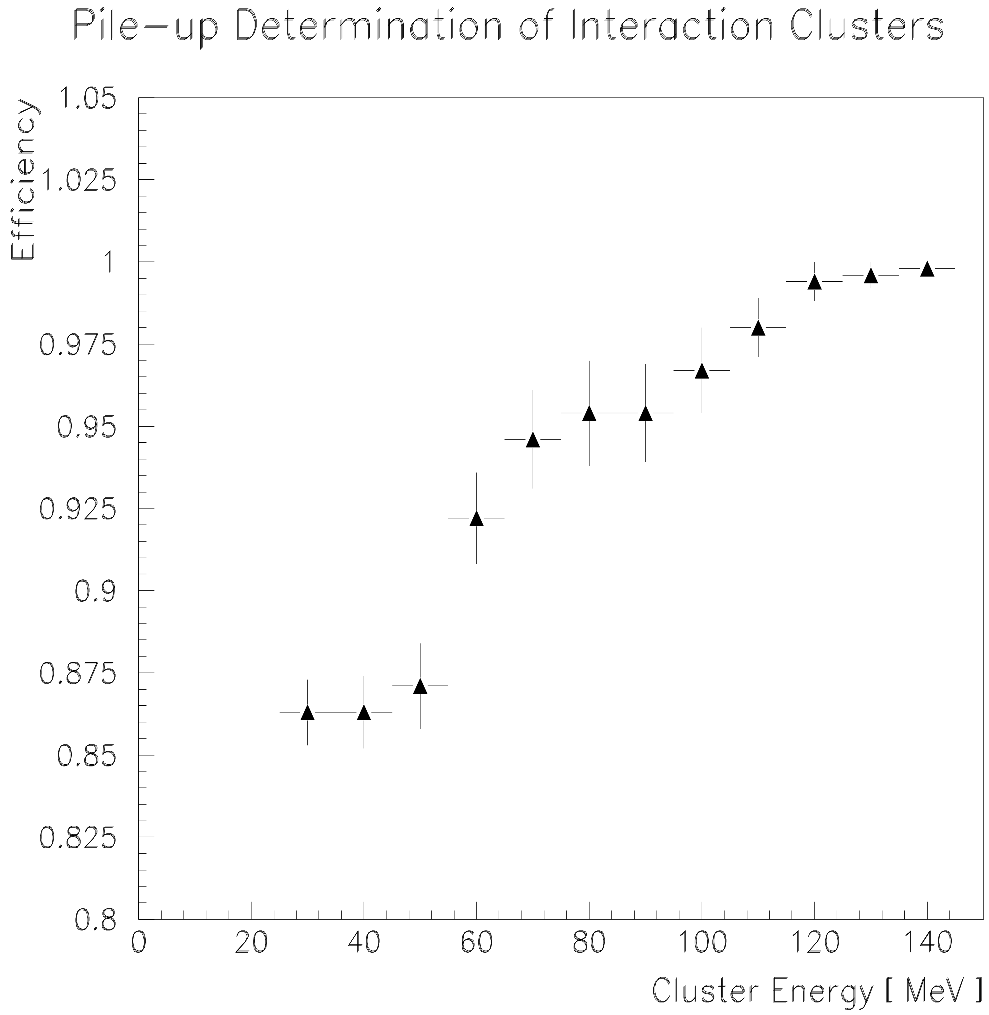

Figure 7.7: The efficiency of the determination of triggered interaction cluster from good $\bar{p}p \rightarrow \pi^o\pi^o$ events as a function of photon cluster energy.

energy, the efficiency of determining an interaction cluster as not being out-time decreases as the energy decreases; at the neutral data analysis threshold, 25 MeV, the efficiency is ≈ 0.85. The loss of events due to the inefficiency of out-time determination of interaction clusters is a function of the frequency that a final state particle will have a low energy cluster; for the $\pi^o\pi^o$ data sample studied, the loss is $\approx 1.5\%$.

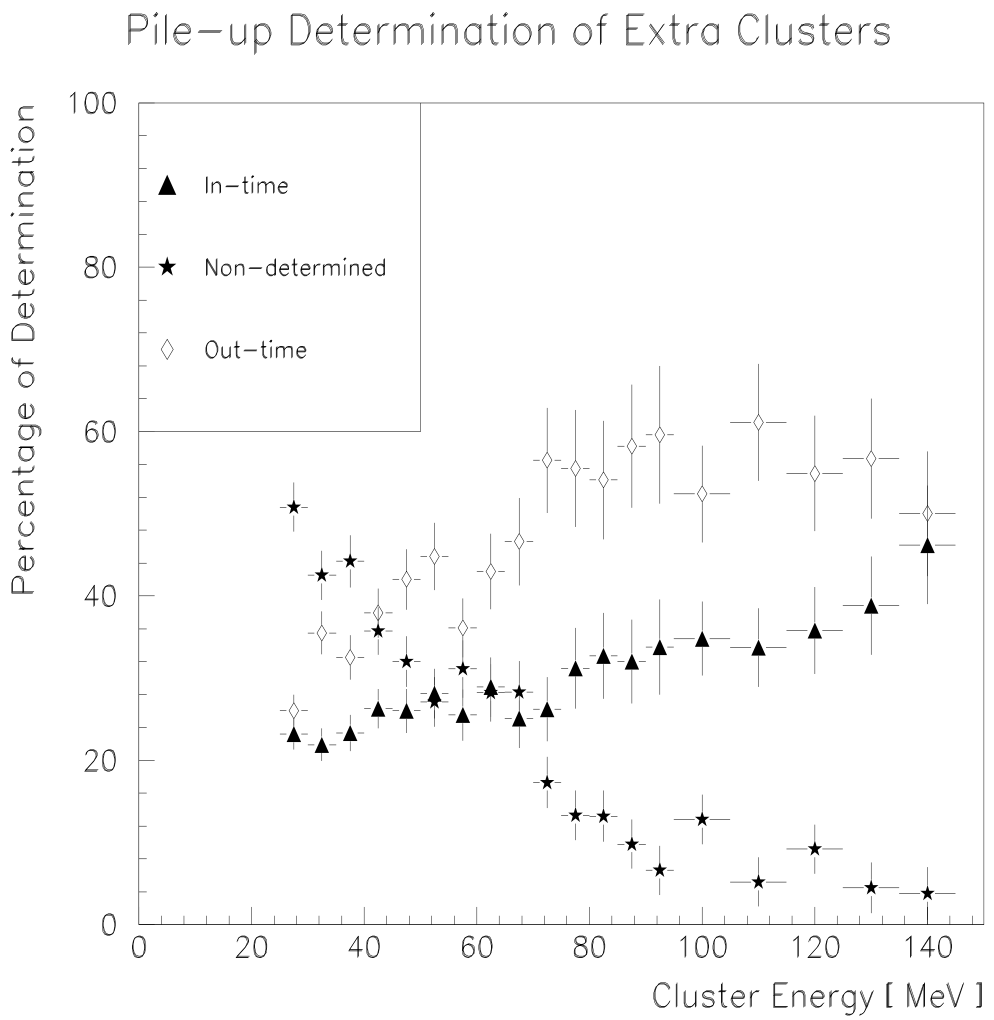

Figure 7.8: The determination percentages of non-triggered interaction signals from good $\bar{p}p \to \pi^o\pi^o$ events as a function of cluster energy: in-time, non-determined, and out-time are the triangles, stars and diamonds, respectively.

The determination of the extra clusters from the good $\pi^o\pi^o$ events is shown in figure 7.8. A fairly large percentage of the extra clusters are declared in-time or non-determined. Table 7.1 shows the number of extra clusters which are declared in-time or non-determined for events which have at least one extra cluster declared as such; table 7.2 shows the largest energy deposit for these extra clusters. The percentage of time that there are extra in-time or non-determined clusters with energies greater

Number of in-time or non-determined extra clusters	Percentage (%)
1	69.1
2	21.6
3	6.3
4	1.7
5	0.9
≥ 6	0.3

Table 7.1: The number of extra clusters which are declared as in-time or non-determined shown as a percentage for events which have at least one extra cluster declared as such.

Energy Range			%	Energy Range			%
25	to	30	12.9	70	to	80	5.2
30		35	10.6	80		90	4.0
35		40	10.5	90		100	3.8
40		45	9.0	100		125	6.1
45		50	7.2	125		150	5.1
50		60	10.3	150		175	3.7
60		70	8.2	175		200	3.6

Table 7.2: The largest energy for the extra clusters which are declared as in-time or non-determined shown as a percentage for events which have at least one extra cluster declared as such.

than 100 MeV in an event is a few percent (1 to 3% for the good $\pi^o\pi^o$ data). These events are probably when two $\bar{p}p$ interactions occur within the timing resolution of the trigger; there is a $\approx 1.7\%$ probability that there is a second interaction which results in a central calorimeter signal (rate of 350 kHz) in a 50 ns window.

7.2 Geometrical Acceptances

The acceptances are dependent upon the angular distribution of the final state. The angular distribution for each channel has been determined using the helicity formalism. A Monte Carlo employing the angular distributions of the reactions gives the geometrical acceptances.

7.2.1 Helicity Formalism

The angular distributions for the reactions have been determined using the helicity formalism [78]. The helicity formalism yields the transition amplitude in terms of the production and decay amplitudes for different helicities. In figure 7.9, diagrams of the $^1\mathrm{P}_1$ reactions, $J/\psi + X$ (with J/ψ decaying to e^+e^-) and $\eta_c + \gamma$, are shown with the helicity formalism parameters; this designation and the method used are described by Richman [79]. The angular distribution is proportional to the amplitude squared when the initial states are averaged over and the final states are

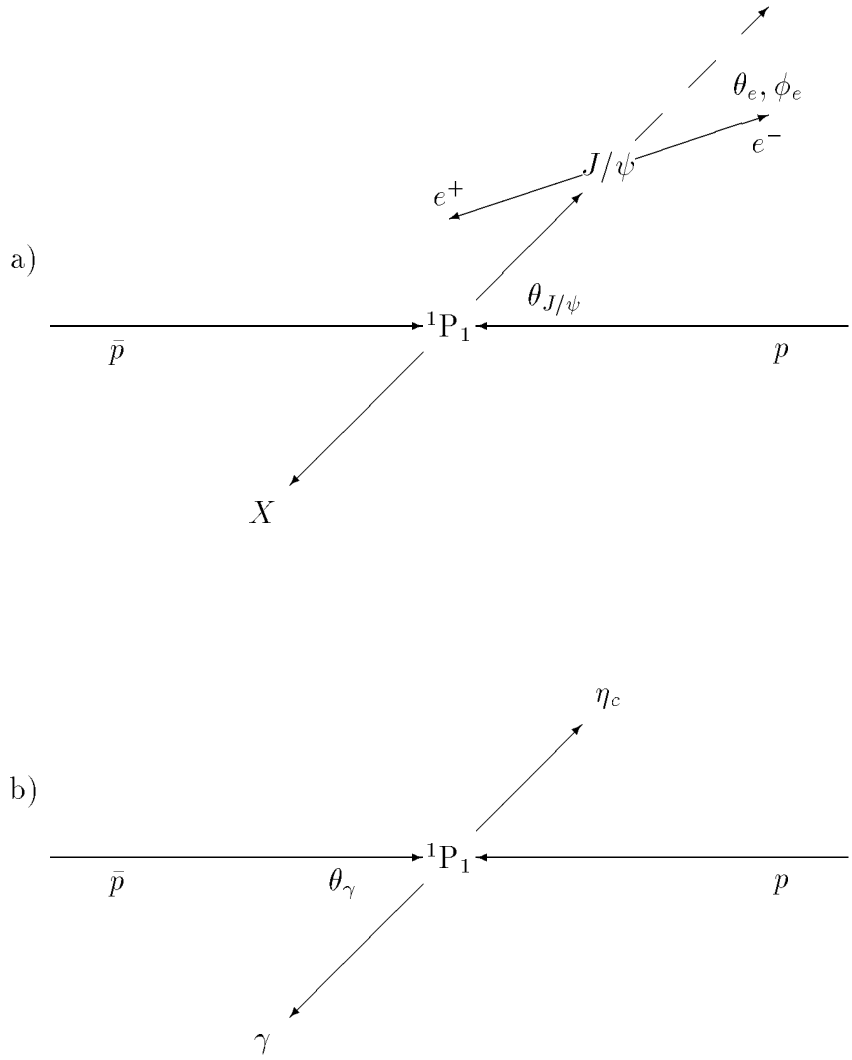

Figure 7.9: Diagrams displaying the $^1\mathrm{P}_1$ reactions and the helicity formalism angles in the center of mass ($\theta_{J/\psi}$ and θ_γ) and the J/ψ rest frame angles (θ_e and ϕ_e): (a) $^1\mathrm{P}_1 \to J/\psi X$ and J/ψ decays to e^+e^- and (b) $^1\mathrm{P}_1 \to \eta_c\gamma$. $\phi_{J/\psi}$ (ϕ_γ) is arbitrary; ϕ_e is 0 when the electron momentum vector is in the same plane as the momentum vectors of the J/ψ and $\bar{p}$.

summed over:

$$\frac{d\sigma}{d\Omega} \propto \sum_{initial} \sum_{final} \mid \mathcal{M} \mid^2 . \tag{7.6}$$

The production amplitude is B_{λ_1,λ_2} where λ_1 and λ_2 are the helicities of the proton and antiproton, respectively. For the charged (neutral) reactions, the decay amplitude is $A_{\mu,\sigma}$ where μ and σ are respectively the helicities of the J/ψ (η_c) and X (γ), where X can be $\pi\pi$ with[2] $J^P = 0^+$ or a π^o. The charged reactions have a further J/ψ decay amplitude of C_{λ_a,λ_b} where λ_a and λ_b are the electron and positron helicities, respectively. The corresponding amplitude for the η_c decay exists but does not affect the final angular distribution since the η_c (as well as π^o, η, and η') decays isotropically.

Each amplitude is normalized such that the sum of the squares of the individual amplitudes is 1 (e.g. $\sum_{\lambda_1,\lambda_2} B^2_{\lambda_1,\lambda_2}$ =1). Due to parity and charge conjugation conservation, there are some relations that the amplitudes must obey. The general parity result for an amplitude M for process $\alpha \to i + j$ is

$$M_{\lambda_i,\lambda_j} = \eta_i \eta_j \eta_\alpha (-1)^{s_i+s_j-s_\alpha} M_{-\lambda_i,-\lambda_j} \tag{7.7}$$

where η and s are the parity and spin of the particle. Parity conservation in the production causes

$$B_{\lambda_1,\lambda_2} = -B_{-\lambda_1,-\lambda_2}, \tag{7.8}$$

resulting in

$$B_{+,-} = -B_{-,+}, \tag{7.9}$$

[2] $J = 0$ is expected to be favored since the phase space is small.

$$B_{+,+} = -B_{-,-}, \tag{7.10}$$

where + and − represent helicities $+\frac{1}{2}$ and $-\frac{1}{2}$, respectively. Meanwhile, charge conjugation in the production only allows

$$B_{\lambda_1,\lambda_2} = B_{\lambda_2,\lambda_1} \tag{7.11}$$

resulting in

$$B_{+,-} = B_{-,+}, \tag{7.12}$$

$$B_{+,+} = B_{+,+}. \tag{7.13}$$

Conditions 7.9 and 7.12 are contradictory for non-zero values of B_1 and B_{-1} ($B_\nu = B_{\lambda_1,\lambda_2}$ and $\nu = \lambda_1 - \lambda_2$); therefore, $B_1 = B_{-1} = 0$ and $B_{+,+} = -B_{-,-}$. Parity conservation of the J/ψ decay and the small mass of the electron and positron result in $C_0 \to 0$ and $C_{+,-} = C_{-,+}$. A constraint due to parity on the decay amplitude occurs for the $J/\psi\pi\pi$ decay of the ${}^1\mathrm{P}_1$; it results in the condition $A_{0,0} = -A_{0,0} = 0$ and $A_{1,0} = -A_{-1,0}$. Since the photon helicity is ± 1, $A_{0,0} = 0$ for $\eta_c\gamma$ and $A_{1,0} = A_{-1,0}$. The parity constraint on the ${}^1\mathrm{P}_1$ decay amplitude to $J/\psi\pi^o$ results in two amplitudes A_0 and A_1 since $A_{\mu,\sigma} = A_{-\mu,-\sigma}$.

In terms of these amplitudes, the transition amplitude of an overall process is given by

$$\mathcal{M} \propto \sum_{\mu} B_{\lambda_1,\lambda_2} A_{\mu,\sigma} D^{J_{h_c}*}_{\lambda_1-\lambda_2,\mu}(\phi_{J/\psi}, \theta_{J/\psi}, -\phi_{J/\psi}) C_{\lambda_a,\lambda_b} D^{J_{J/\psi}*}_{\mu,\lambda_a-\lambda_b}(\phi_e, \theta_e, -\phi_e), \tag{7.14}$$

where the J/ψ subscript refers to the J/ψ direction with respect to the $\bar{p}$ direction in the center of mass frame and the e subscript refers to the electron direction in the

J/ψ rest frame with respect to the J/ψ boost direction. The $\eta_c\gamma$ overall amplitude does not have the last two factors and the gamma ray direction is substituted for the J/ψ direction. Applying the constraints mentioned above, working through the algebra and keeping track of all the terms, the angular distribution, or the form of the differential cross section, is determined. The simplest is the $\eta_c\gamma$ decay of the $^1\mathrm{P}_1$:

$$\frac{d\sigma}{d\Omega} \propto \sin^2\theta_\gamma. \tag{7.15}$$

The $^1\mathrm{P}_1$ decay to $J/\psi\pi\pi$ with $J/\psi \to e^+e^-$ angular distribution is

$$\frac{d\sigma}{d\Omega} \propto \sin^2\theta_{J/\psi}(1+\cos^2\theta_e) + \sin^2\theta_{J/\psi}\sin^2\theta_e\cos(2\phi_{J/\psi} - 2\phi_e). \tag{7.16}$$

The $J/\psi\pi^o$ with $J/\psi \to e^+e^-$ angular distribution involves unknown $^1\mathrm{P}_1$ decay amplitudes:

$$\begin{aligned}\frac{d\sigma}{d\Omega} \propto \quad & A_1^2 sin^2\theta_{J/\psi}(1+\cos^2\theta_e) - A_1^2\sin^2\theta_{J/\psi}\sin^2\theta_e\cos(2\phi_{J/\psi} - 2\phi_e) \\ & +2A_0^2\cos^2\theta_{J/\psi}\sin^2\theta_e + A_1A_0\sin 2\theta_{J/\psi}\sin 2\theta_e\cos(\phi_{J/\psi} - \phi_e).\end{aligned} \tag{7.17}$$

7.2.2 Monte Carlo

An event Monte Carlo has been developed which generates events with the appropriate angular distribution for a reaction. The energies and positions of the final particles are also generated to simulate the detector's resolutions. The appropriate geometrical and energy threshold cuts that are applied during the analysis are made and an acceptance is determined. The inclusive J/ψ and 3γ final state acceptance α_{geom} are presented in table 7.3. The range of acceptances for the $J/\psi\pi^o$ final state

Final State	Acceptance
$J/\psi\pi^+\pi^-$	0.239
$J/\psi\pi^o\pi^o$	0.192
$J/\psi\pi^o$	0.32 to 0.54
$\eta_c\gamma \to 3\gamma$	0.368

Table 7.3: The geometrical acceptances of the inclusive J/ψ and 3γ final states. The range of values for the $J/\psi\pi^o$ final state is for a range of the ${}^1\mathrm{P}_1$ decay helicity amplitudes.

is for a range of ${}^1\mathrm{P}_1$ decay helicity amplitudes. The 7γ final state acceptances are in table 7.10.

7.3 Trigger Efficiencies

Both the hardware and software trigger requirements contribute to the trigger efficiencies. Each of the trigger bits that have a requirement for a trigger contributes to the total trigger efficiency. Efficiencies resulting from requiring a bit to be ON or OFF are discussed below. Common to both the charged and neutral hardware triggers is the coplanarity of large energy deposits in the central calorimeter bit, PBG. From the J/ψ and ψ' data sets, ϵ_{PBG} is essentially 1.0.

7.3.1 Charged Trigger

The main contribution to the inefficiency of the charged trigger is due to space between elements of the H1 and H2 hodoscopes. Charged particles which do not hit an element of the H1 or H2 hodoscopes do not form a charge track in the trigger.

Charged tracks (with signals in both H1 and H2) which are not the charged particles which formed the trigger, have been plotted as a function of ϕ in figure 7.10 (all H2 elements are superimposed onto one element). The efficiency of requiring the hadron hardware trigger bit to be ON is given by the deficit of hits at the edges of the H2 element,

$$\epsilon_h = 0.961 \pm 0.005. \tag{7.18}$$

The efficiency of requiring the two hadron hardware trigger bit to be ON for charged non-two body final states is

$$\epsilon_{hh} = \epsilon_h^2 = 0.924 \pm 0.01. \tag{7.19}$$

Extra hit elements of the H1 and H2 hodoscopes also contribute to inefficiencies of the charged trigger. Clean samples of J/ψ and inclusive J/ψ from the χ_2 resonance data are used to see how often the trigger bits (H1$>$ 2, H2$>$ 2) are ON indicating an extra hodoscope element has been hit. Events are selected based upon satisfying the two electron trigger (see logic statement 5.7); the pattern units associated with the MLUs are checked for the status of each of the bits. The ≈ 3600 J/ψ (≈ 1400 χ_2) events are split into data sets of ≈ 900 (350) events to study rate effects. Figures 7.11 and 7.12 show the efficiency of vetoing on the H1$>$ 2 and H2$>$ 2 bits, respectively, as a function of each hodoscope's rate. A fit gives the efficiency resulting from vetoing on the H1$>$ 2 bit status in the pattern unit as

$$\epsilon_{H1} = (1.020 \pm 0.009) - (0.097 \pm 0.009) \times (\text{H1 OR rate in MHz}); \tag{7.20}$$

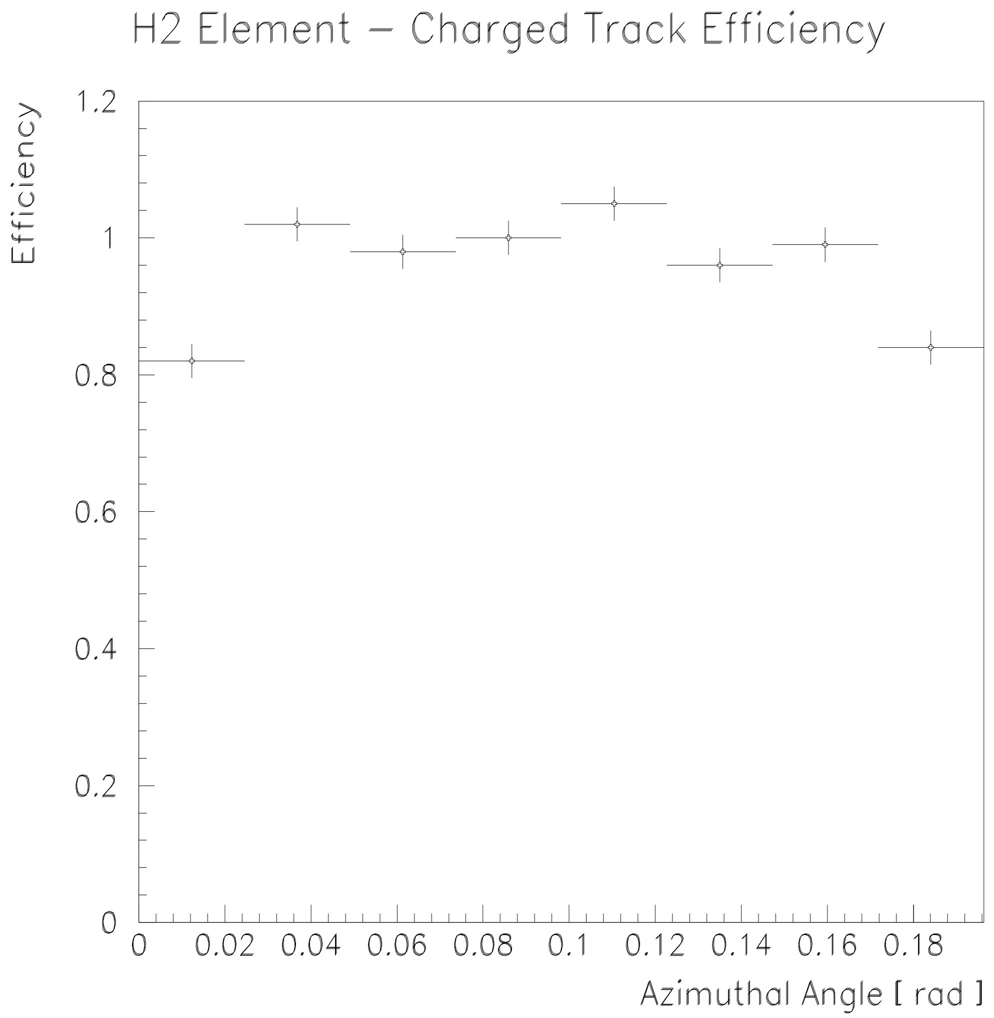

Figure 7.10: The efficiency of the hadron hardware trigger bit is seen by the decrease of the number of tracks at the edges of an H2 element (all H2 elements are superimposed onto one H2 element) as compared to the number that cross the center of an H2 element.

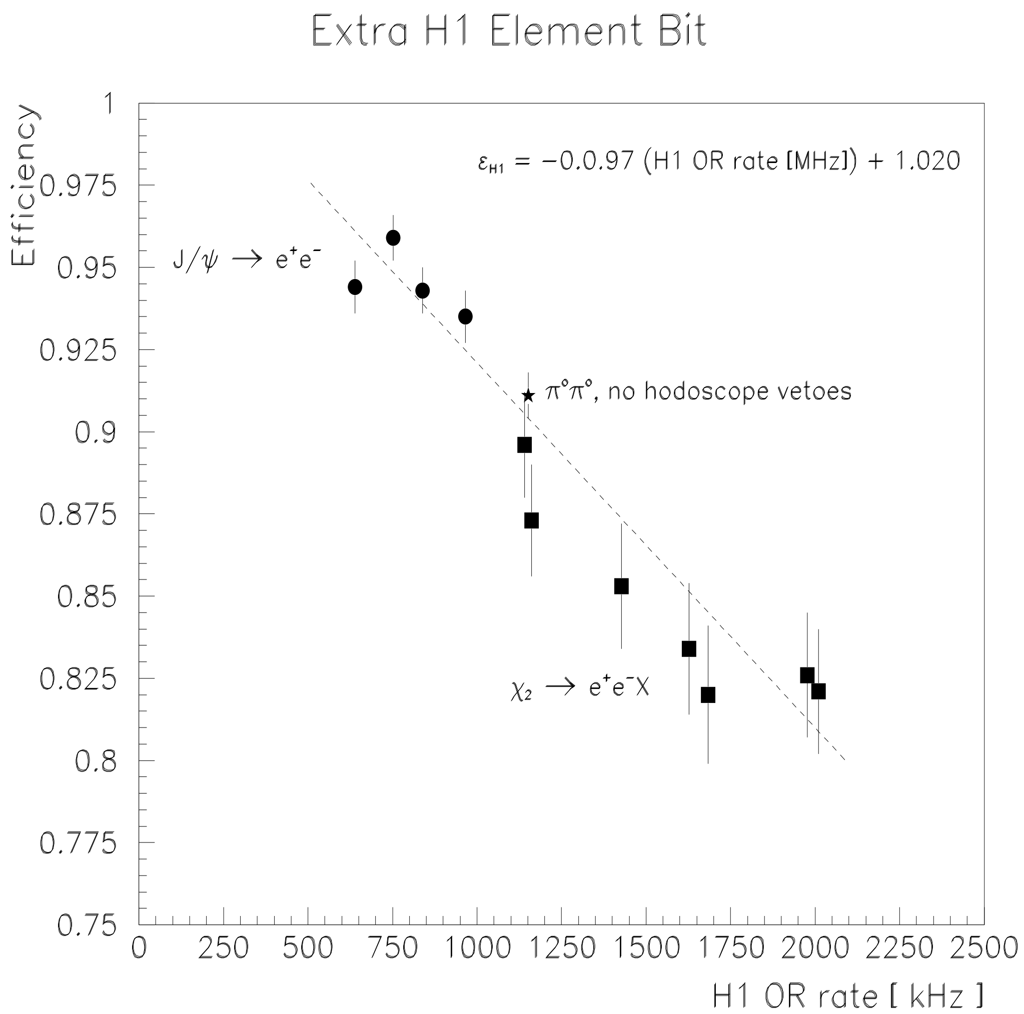

Figure 7.11: The efficiency resulting from vetoing on the pattern unit information as a function of the H1 OR rate for extra H1 element bits: charged events – vetoing on the H1>2 information for events collected with the two electron trigger at the J/ψ (circles) and χ_2 (squares) resonances; neutral events – H1 OR information for $\pi^o\pi^o$ events (star) collected when no hodoscopes are used as vetoes.

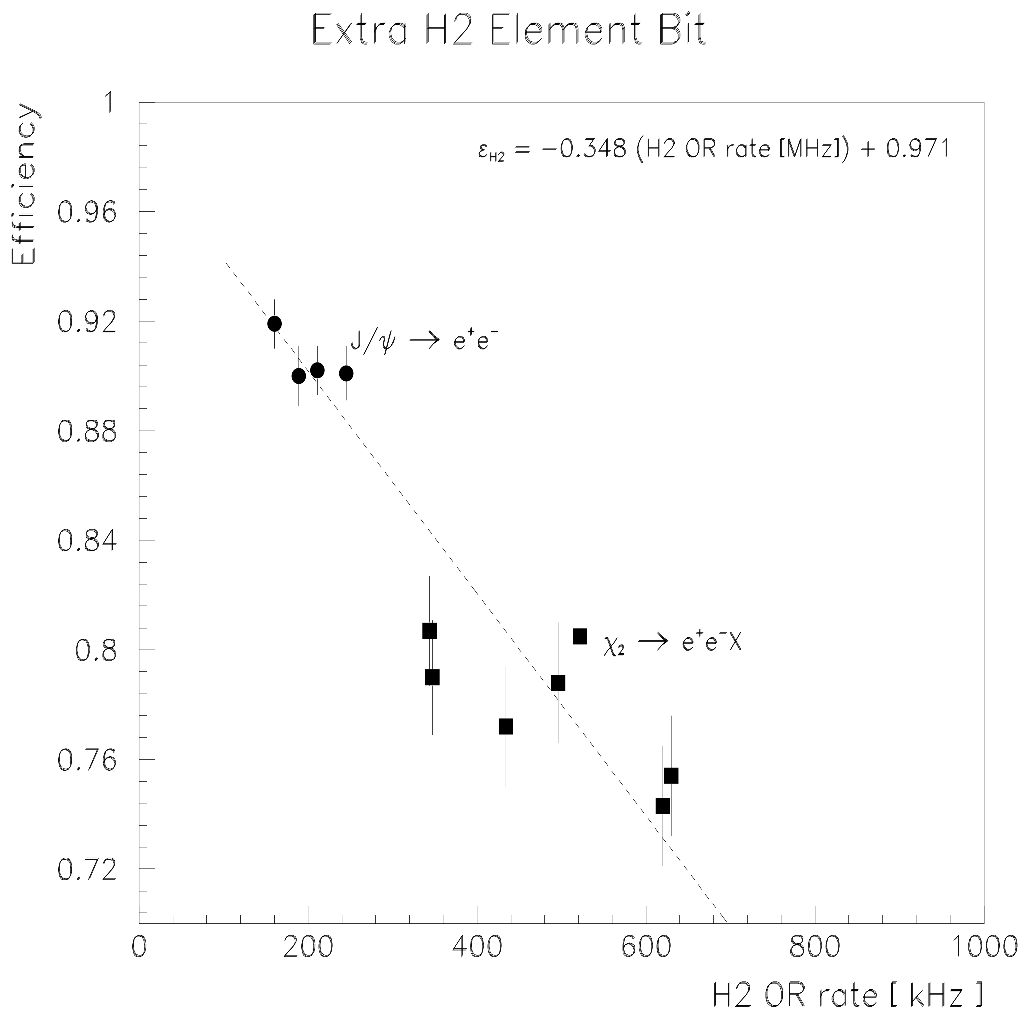

Figure 7.12: The efficiency resulting from vetoing on the pattern unit information as a function of the H2 OR rate for extra H1 element bits: vetoing on the H2> 2 information for events collected with the two electron trigger at the J/ψ (circles) and χ_2 (squares) resonances.

Stack Number	H1 OR rate min	max	ave	H2 OR rate min	max	ave
1	787	2188	1439	229	656	436
2	901	1926	1421	265	595	429
3	582	1726	1182	168	528	353
4	848	1631	1264	249	500	380
5	1145	2257	1747	336	707	529
6	999	2296	1617	289	708	486
7	1078	2324	1644	315	685	494
8	1048	2381	1712	302	742	516
9	1167	2300	1765	397	691	532
10	1412	2292	1782	413	714	536
11	1388	2004	1693	414	609	507
12	976	1799	1477	292	540	440
13	1350	2212	1776	396	685	535
14	1260	2022	1647	366	616	491
15	1448	2211	1847	424	683	557
16	1833	2364	2031	555	702	616

Table 7.4: The H1 and H2 rates for each stack. All rates are in kHz.

for H2> 2 the fit is

$$\epsilon_{H2} = (0.971 \pm 0.009) - (0.348 \pm 0.030) \times (\text{H2 OR rate in MHz}). \tag{7.21}$$

One datum point of figure 7.11 is from the efficiency resulting from vetoing on the H1 OR bit's status in the pattern unit for a special neutral trigger (see next section); the results are in agreement. Table 7.4 shows the minimum, maximum and average rates for each $^1P_1$ stack for the H1 OR and H2 OR.

The efficiency resulting from vetoing on the extra H1 bit due to information from the pattern unit needs to be corrected. The pattern unit's gate width is 30 ns while the strobe to the trigger deciding MLUs is 5 ns wide. Therefore, it is possible that a bit is OFF when the MLU makes a decision, but the pattern unit has the bit ON; this means that ϵ_{H1} underestimates the efficiency resulting from vetoing on the

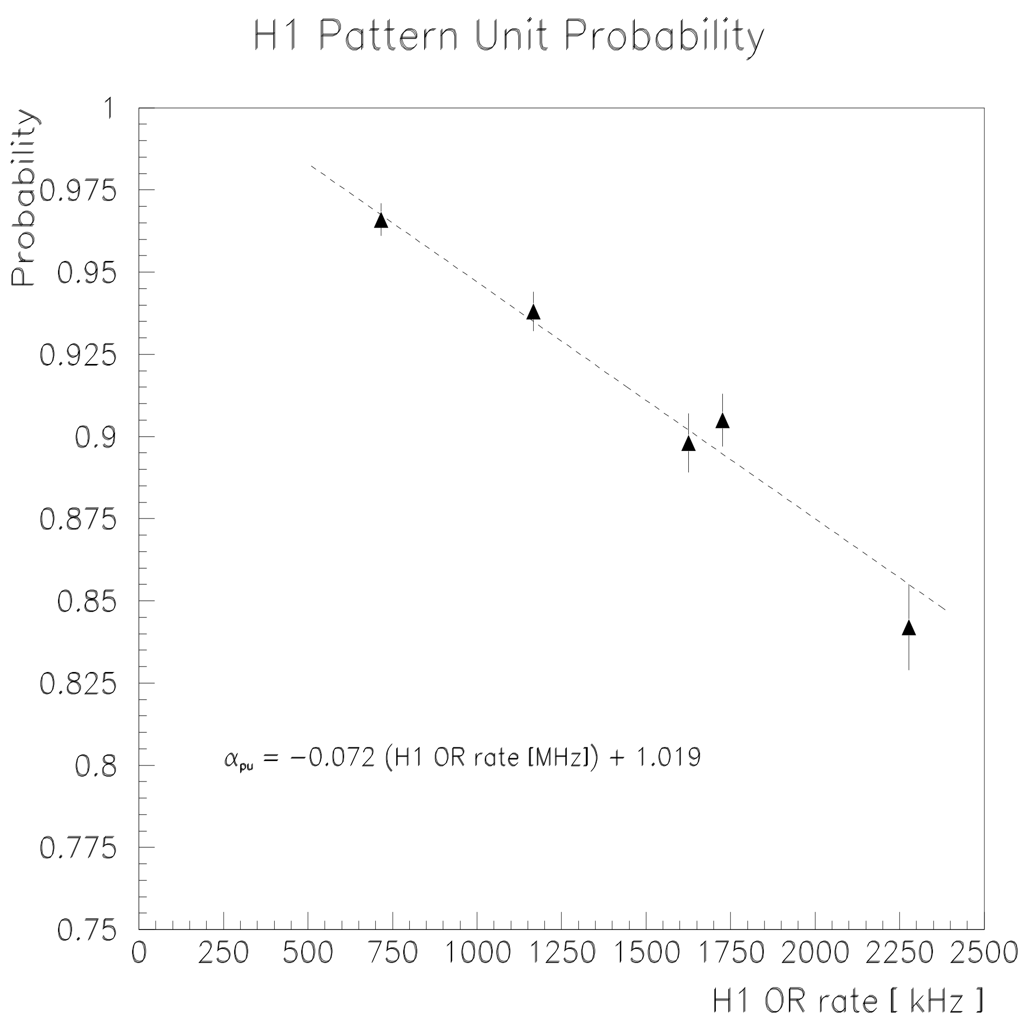

Figure 7.13: The probability that a pattern unit correctly shows the H1 OR bit OFF for $\bar{p}p \rightarrow \pi^o\pi^o$ as a function of the H1 OR rate.

extra H1 element bits in the trigger. A correction is made using the probability that the pattern unit correctly shows the bit being OFF when the trigger vetoes on the bit. The probability of the correct designation of the H1 OR bit in the pattern unit for $\bar{p}p \rightarrow \pi^o\pi^o$ is shown as a function of rate in figure 7.13. A fit gives the probability as

$$\alpha_{pu} = (1.019 \pm 0.009) - (0.072 \pm 0.009) \times (\text{H1 OR rate in MHz}). \qquad (7.22)$$

Final State	ϵ_{COPL}
$J/\psi\pi^+\pi^-$	0.999
$J/\psi\pi^o\pi^o$	0.999
$J/\psi\pi^o$	0.929

Table 7.5: The coplanarity bit efficiencies for different reactions as determined by an event generating Monte Carlo.

The corrected trigger efficiency resulting from vetoing on an extra H1 element bit is $\frac{\epsilon_{H1}}{\alpha_{pu}}$. All other trigger bits investigated in this chapter (H2> 2, FCH OR, and FCAL OR) have negligible corrections; less than 0.2% of the events have the pattern unit ON for a bit when the trigger required the bit OFF.

The efficiency of the H2=2 bit being ON is the same as the efficiency resulting from vetoing on the H2> 2 bit. The efficiencies resulting from vetoing on the hodoscope bits in the two electron trigger, H1> 4 and H2> 4 bits, are related to the cubes of the inefficiencies[3] of the H1> 2 and H2> 2 bits:

$$\epsilon'_{H1} = 1 - (1 - \frac{\epsilon_{H1}}{\alpha_{pu}})^3, \tag{7.23}$$

$$\epsilon'_{H2} = 1 - (1 - \epsilon_{H2})^3. \tag{7.24}$$

The efficiency of the coplanarity requirement is determined from the event generating Monte Carlo discussed in the last section and the values are shown in table 7.5.

The hardware trigger identification of electrons and positrons is dependent upon the polar angle of the particle. The J/ψ data set is used to study the effect of the Čerenkov septum at $\theta_{lab} = 38°$. At the J/ψ, when the electron enters the septum

[3]H1> 4 and H2> 4 require three *separate* extra hodoscope elements to be hit; therefore, ϵ'_{H1} and ϵ'_{H2} are underestimated, however, any corrections would be small since $\epsilon'_{H2} = 0.98$ when $\epsilon_{H2} = 0.75$.

region the positron does also, since the septum for J/ψ data corresponds to $\cos\theta_{cm} = 0$; however for a $^1\mathrm{P}_1$ event, the Monte Carlo never has both the electron and positron in the septum region. Data taking at the J/ψ included a provision for both particles near the septum with a zero electron trigger along with the one and two electron triggers described in section 5.3. A comparison of the e^+e^- events acquired by the zero and two electron triggers with all other inefficiencies removed results in a determination of the two electron bit efficiency to be

$$\epsilon_{ee} = 0.88 \pm 0.01. \tag{7.25}$$

The one electron bit efficiency, ϵ_e, is found to be ≈ 1.0.

Since the charged trigger events are passed by the ACP slave node program, there is no software trigger inefficiency. The total trigger efficiency for the charged events can be written as

$$\begin{aligned} \epsilon_{trig} = \quad & \epsilon_{PBG} \times \epsilon_{hh} \times [\epsilon_{ee} \times \epsilon'_{H1} \times \epsilon'_{H2} + \\ & (1 - \epsilon_{ee} \times \epsilon'_{H1} \times \epsilon'_{H2}) \times \epsilon_e \times \tfrac{\epsilon_{H1}}{\alpha_{pu}} \times \epsilon_{H2} \times \epsilon_{COPL}] \end{aligned} \tag{7.26}$$

when there are only two charged particles in the final state. When there are four charged particles in the final state, the second term in the square brackets is dropped and the H1 and H2 efficiencies of the first term change from ϵ'_{H1} and ϵ'_{H2} to $\frac{\epsilon_{H1}}{\alpha_{pu}}$ and ϵ_{H2}, respectively. The total trigger efficiences are

$$\epsilon_{trig}(J/\psi\pi^o) = \epsilon_{trig}(J/\psi\pi^o\pi^o) = 0.89, \tag{7.27}$$

$$\epsilon_{trig}(J/\psi\pi^+\pi^-) = 0.37, \tag{7.28}$$

when average values for the H1 OR and H2 OR rates from the $^1P_1$ data taking are used (see table 7.4). The $\epsilon_{trig}(J/\psi\pi^+\pi^-)$ takes into account the requirement that the pions and e^+e^- are not in contiguous H2 hodoscope elements. During a stack, the trigger efficiency changes by less than 1% for the $J/\psi\pi^o$ and $J/\psi\pi^o\pi^o$ final states; the range for the $J/\psi\pi^+\pi^-$ trigger efficiency is 0.32 to 0.44 and the luminosity averaged values for the stacks range from 0.35 to 0.40.

7.3.2 Neutral Trigger

The inefficiencies of the neutral hardware trigger result from the vetoes on the detector component bits. The H1 efficiency found for the charged trigger (the extra hodoscope element hit) is the same for the neutral trigger. To confirm this, one data run has been taken with no vetoes of the H1 OR bit or the FCH OR bit required for the neutral trigger. The frequency of the H1 OR bit being ON in the pattern unit for reconstructed $\bar{p}p \rightarrow \pi^o\pi^o$ events is 14.5%. Each π^o has the probability of Dalitz decay of 1.2% and each photon has an $\approx 1.0\%$ probability of converting in the beam pipe before the H1 hodoscope, $\alpha_{convert}$; the accidental H1 rate is corrected to be 8.8%. This datum point is included in figure 7.11.

The forward hodoscope bit (FCH OR) is ON for 3.5% of the $\pi^o\pi^o$ events collected without the hodoscope vetoes[4]. The rate dependence of the FCH OR bit has also been studied using the same charged event data sets as have been used above for

[4]These events are independent of the events for which the H1 OR bit is ON.

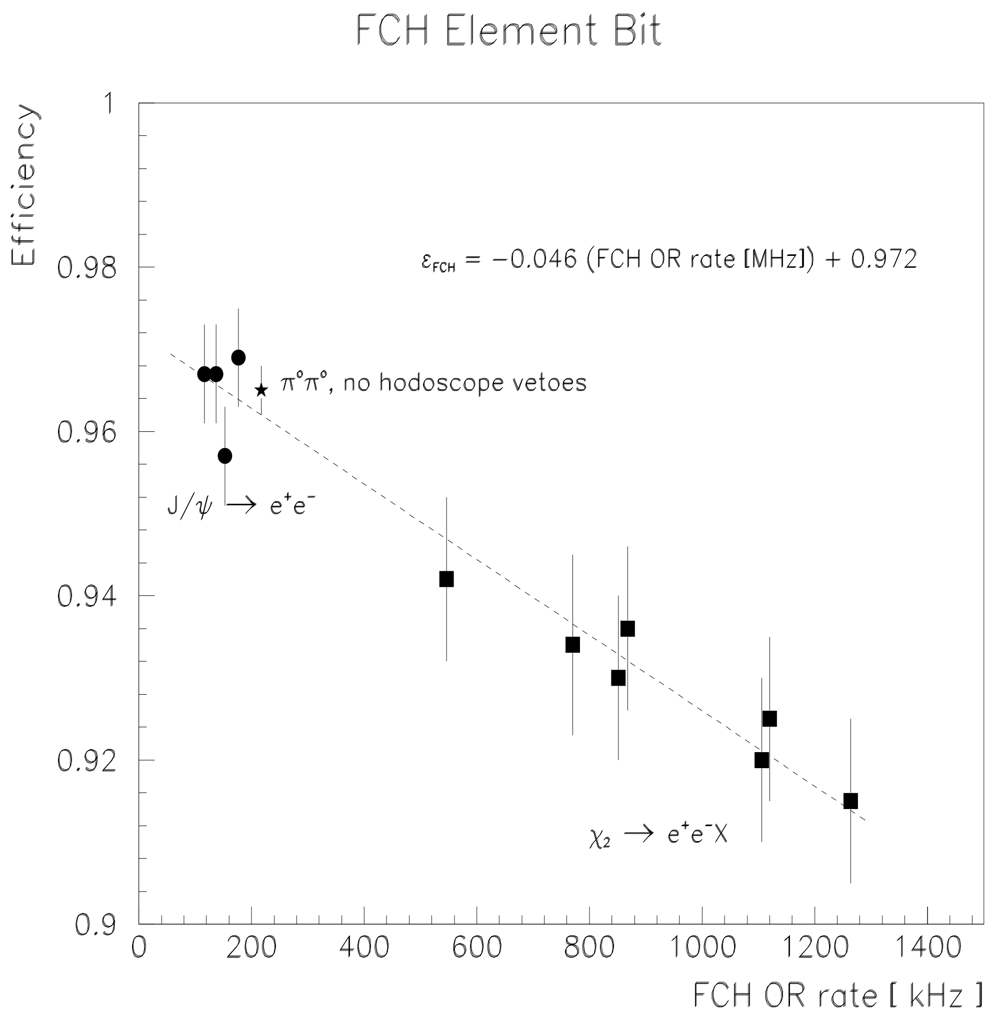

Figure 7.14: The efficiency resulting from vetoing on the FCH OR bit as a function of the FCH OR rate: charged events – events collected with the two electron trigger at the J/ψ (circles) and χ_2 (squares) resonances; neutral events – $\pi^o\pi^o$ events (star) collected when no hodoscopes are used as vetoes.

Stack Number	FCH OR rate min	FCH OR rate max	FCH OR rate ave	FCAL OR rate min	FCAL OR rate max	FCAL OR rate ave
1	455	1026	754			
2	612	1136	880			
3	467	1221	885	510	1190	900
4	561	964	764	710	1120	960
5	239	498	380	890	1420	1180
6	198	489	333	621	1141	903
7	223	472	343	734	1200	1003
8	209	510	355	806	1327	1089
9	259	489	382	532	873	739
10	288	491	372	577	915	723
11	301	421	356	605	796	693
12	217	376	315	431	723	612
13	275	473	372	539	877	710
14	254	425	340	485	774	636
15	293	472	386	563	854	724
16	397	486	432	749	874	801

Table 7.6: The forward hodoscope and calorimeter rates for each stack. All rates are in kHz. Vetoing on the FCAL OR bit was not done until the 3^{rd} stack and the FCAL OR rate is estimated before the 6^{th} stack. The forward hodoscope (calorimeter) was improved after the 4^{th} (8^{th}) stack reducing the rate.

studying the other hodoscopes, excluding χ_2 events where the gamma ray goes into the forward calorimeter. Figure 7.14 shows the rate dependence and the resulting fit for the efficiency resulting from vetoing on the FCH OR bit is

$$\epsilon_{FCH} = (0.973 \pm 0.003) - (0.046 \pm 0.005) \times (\text{FCH OR rate in MHz}). \qquad (7.29)$$

The minimum, maximum and average FCH OR rates for each $^1P_1$ stack is shown in table 7.6.

The forward calorimeter veto of 7γ final state events has a rate dependence. The efficiency resulting from vetoing on the FCAL OR bit for events collected with the two electron trigger at the J/ψ resonance and good $\pi^o\pi^o$ events (section 7.1.2)

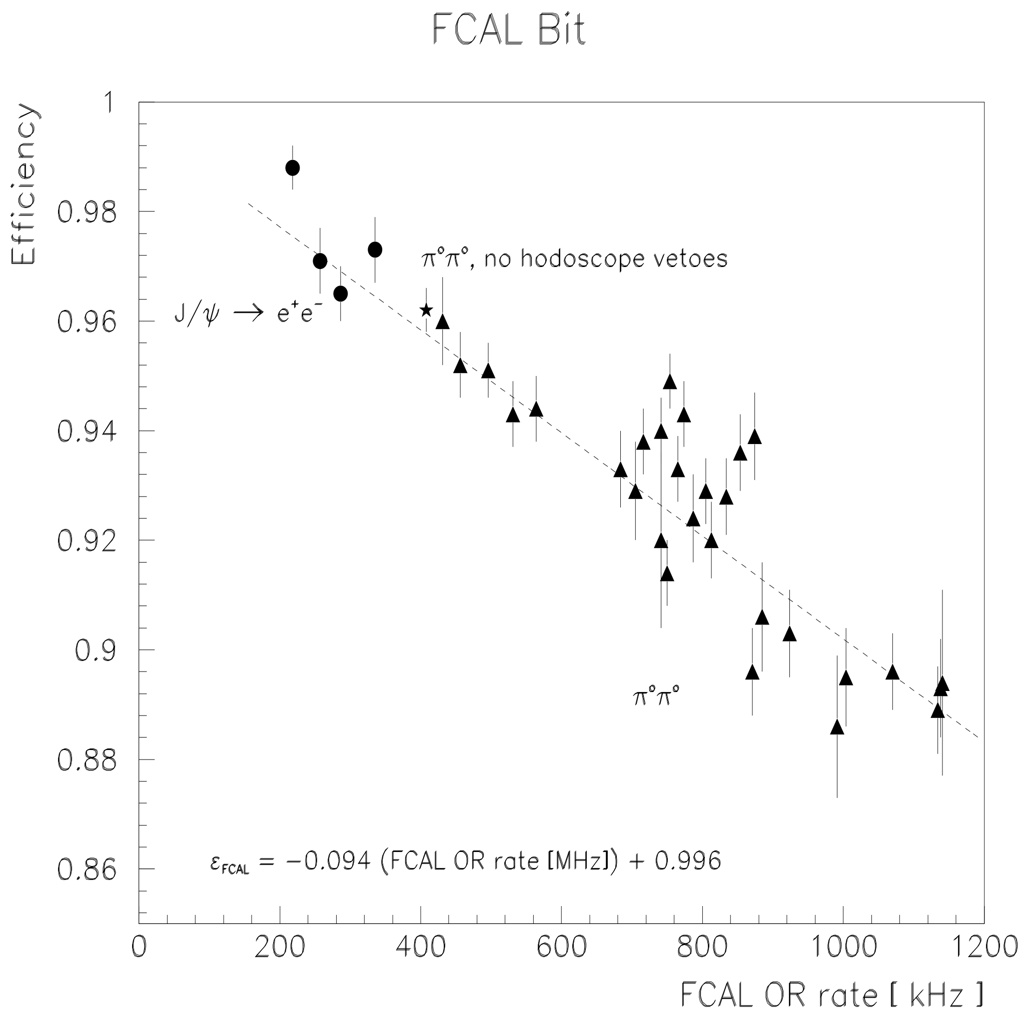

Figure 7.15: The efficiency resulting from vetoing on the FCAL OR bit as a function of the FCAL OR rate: charged events – events collected with the two electron trigger at the J/ψ (circles) resonance; neutral events – good $\pi^o\pi^o$ events (triangles).

Stack	$\epsilon_{ETOT-hard}$	$\epsilon_{ETOT-soft}$	Stack	$\epsilon_{ETOT-hard}$	$\epsilon_{ETOT-soft}$
1	1.00	1.00	9	0.98	0.98
2	1.00	1.00	10	0.97	0.99
3	1.00	1.00	11	0.97	0.98
4	1.00	1.00	12	0.96	0.98
5	1.00	0.98	13	0.96	0.98
6	0.99	0.98	14	0.96	0.97
7	0.99	0.99	15	0.95	0.97
8	0.98	0.99	16	0.96	0.96

Table 7.7: The efficiency of the hardware and software ETOT trigger bits for each stack.

is shown in figure 7.15. The rate dependent efficiency resulting from vetoing on the FCAL OR bit is

$$\epsilon_{FCAL} = (0.996 \pm 0.006) - (0.094 \pm 0.007) \times (\text{FCAL OR rate in MHz}). \qquad (7.30)$$

The minimum, maximum and average FCAL OR rates[5] for each $^1P_1$ stack is shown in table 7.6.

The collection of 7γ final states relies upon triggering the hardware ETOT bit while the FCAL OR bit is OFF. The efficiency of the ETOT bit has been studied with the selection of good $\pi^o\pi^o$ events. A stack dependence has been found and the efficiency of the hardware ETOT and the efficiencies are presented in table 7.7. The decrease of efficiency of the hardware ETOT trigger bit over time is due to the slow decrease of the central calorimeter counters' gains.

The ACP slave node program affects the 3γ and 7γ events differently. The 3γ final state should satisfy the software trigger's $>$ 2 GeV invariant mass bit. The

[5]The FCAL OR bit was not available in the trigger until the 3^{rd} stack and the FCAL OR rate is estimated before the 6^{th} stack.

software efficiency for the 3γ state is estimated to be

$$\epsilon_{INV} = 0.995 \pm 0.002; \tag{7.31}$$

the inefficiency is due to the simplistic clustering and energy corrections performed in the ACP slave node program as well as the gain constants that are loaded. The 90% total energy software trigger is influenced more by the gain constants that are loaded into the ACP slave node program. The gain constants have been updated every few stacks; however near the end of the 1991 data run, the gain constants remained unchanged. The efficiency of the software ETOT trigger bit has also been studied for each stack and the values are presented in table 7.7 after removal of the hardware ETOT bit inefficiency.

The trigger efficiency for the 3γ final state is

$$\epsilon_{trig}(3\gamma) = \epsilon_{PBG} \times \frac{\epsilon_{H1}}{\alpha_{pu}} \times \epsilon_{FCH} \times \epsilon_{INV} \times (1 - \alpha_{convert})^3 \tag{7.32}$$

where a factor $\alpha_{convert}$ is included for each photon. When average rates are used, $\epsilon_{trig}(3\gamma) = 0.88$. The range of efficiencies goes from 0.85 to 0.91 and the luminosity weighted averages for a stack range from 0.87 to 0.89.

The 7γ final state trigger efficiency is given by

$$\epsilon_{trig}(7\gamma) = \frac{\epsilon_{H1}}{\alpha_{pu}} \times \epsilon_{FCAL} \times \epsilon_{ETOT-hard} \times \epsilon_{ETOT-soft} \times (1 - \alpha_{convert})^7, \tag{7.33}$$

where the individual run efficiencies are rate and stack dependent. The trigger efficiency for the 7γ final states using the average rates is 0.78. The range of efficiencies goes from 0.72 to 0.87 and the luminosity weighted averages for a stack range from 0.74 to 0.82.

7.4 Analysis Efficiencies

A common cut to both the charged and neutral analyses is the cluster mass cut. Figure 7.5 shows that the efficiency of requiring $M_{cl} < 100$ MeV/c^2 for a large energy deposit is

$$\epsilon_{cl} = 0.961 \pm 0.009 \tag{7.34}$$

for $\psi' \to e^+e^-$ events. The cluster mass cut on 7γ final states mainly removes events where two of the gamma rays are close to one another; the energies of the neutral mesons are small enough that most of the two photon decays result in isolated clusters.

7.4.1 Charged Analysis

The major charged analysis cut involves the product of $EQW_1 \times EQW_2$ (see section 6.5). The cut has an efficiency of

$$\epsilon_{EQW} = 0.906 \pm 0.011 \tag{7.35}$$

from study of J/ψ and ψ' data. The electron quality weight cut is redundant with the cluster mass cut; the latter is not used for the electron clusters. The unassociated cluster cut efficiency is estimated to be

$$\epsilon_{ucc} = 0.97 \pm 0.01; \tag{7.36}$$

unassociated in-time and non-determined clusters above 100 MeV are from two nearly simultaneous $\bar{p}p$ interactions. This results in the inclusive J/ψ selection efficiency of

$$\epsilon_{inc} = \epsilon_{EQW} \times \epsilon_{ucc} = 0.88 \pm 0.014. \tag{7.37}$$

Final State	ϵ_{an}
$J/\psi\pi^o$	0.83 ± 0.02
$J/\psi\pi^o\pi^o$	0.73 ± 0.02
$J/\psi\pi^+\pi^-$	0.75 ± 0.03

Table 7.8: The final charged analysis efficiencies. The contiguous H2 cut for the charged pions is not included; it is accounted for in the trigger efficiency.

The efficiency of the pile-up determination for the gamma ray final states has been simulated by the event Monte Carlo; the efficiency is $\epsilon_{pile} = 0.987 \pm 0.005$ (0.941) for the $J/\psi\pi^o$ ($J/\psi\pi^o\pi^o$) final state. The charged pions are only subjected to the pile-up cut if the pion results in any kind of signal in the central calorimeter[6]; the efficiency is estimated as $\epsilon_{pile} = 0.95 \pm 0.02$ for the $J/\psi\pi^+\pi^-$ final state. Each gamma ray is subjected to the cluster mass cut and contributes to the analysis efficiency. The efficiency of requiring two good charged tracks for the charged pions is estimated to be $\epsilon_{tracks} = 0.90 \pm 0.02$. The efficiency of the H2 contiguous cut for the charged pions is included in the determination of the trigger efficiency.

The final charged analysis efficiency is given by

$$\epsilon_{an} = \epsilon_{inc} \times \epsilon_{pile} \times \epsilon_{tracks} \times (\epsilon_{cl})^{\#\gamma}. \tag{7.38}$$

Efficiencies of the charged analyses are presented in table 7.8.

[6]Approximately 73% of the $\psi' \to J/\psi\pi^+\pi^-$ events have central calorimeter clusters associated with the charged pion tracks.

Stack Number	CCAL OR rate min	max	ave	Stack Number	CCAL OR rate min	max	ave
1	157	461	302	9	258	478	377
2	187	434	304	10	285	485	368
3	118	373	246	11	299	415	352
4	180	363	275	12	216	372	313
5	237	493	372	13	272	468	368
6	196	480	329	14	250	420	335
7	219	475	339	15	288	464	379
8	205	500	349	16	385	476	421

Table 7.9: The central calorimeter rates for each stack. All rates are in kHz.

7.4.2 Neutral Analysis

The neutral analysis efficiencies are not as straight forward as the charged analysis efficiencies. The extra cluster cut is rate dependent; the efficiency of the cut as a function of the central calorimeter rate for the good $\pi^o\pi^o$ events is shown in figure 7.16. The rate dependence of the extra cluster cut efficiency is

$$\epsilon_{ecc} = (0.911 \pm 0.006) - (0.278 \pm 0.020) \times (\text{CCAL OR rate in MHz}). \qquad (7.39)$$

Table 7.9 shows the minimum, maximum and average CCAL OR rate for the $^1P_1$ stacks[7].

The cut of no forward calorimeter clusters affects the 3γ and 7γ analyses differently due to the presence of the veto on the FCAL OR bit in the trigger for 7γ events. Figure 7.17 shows the forward calorimeter cluster cut efficiency as a function

[7]There was a problem in the production of the stack 16 neutral DSTs resulting in a rate independent central calorimeter extra cluster cut efficiency of $\epsilon_{ecc} = 0.52 \pm 0.02$.

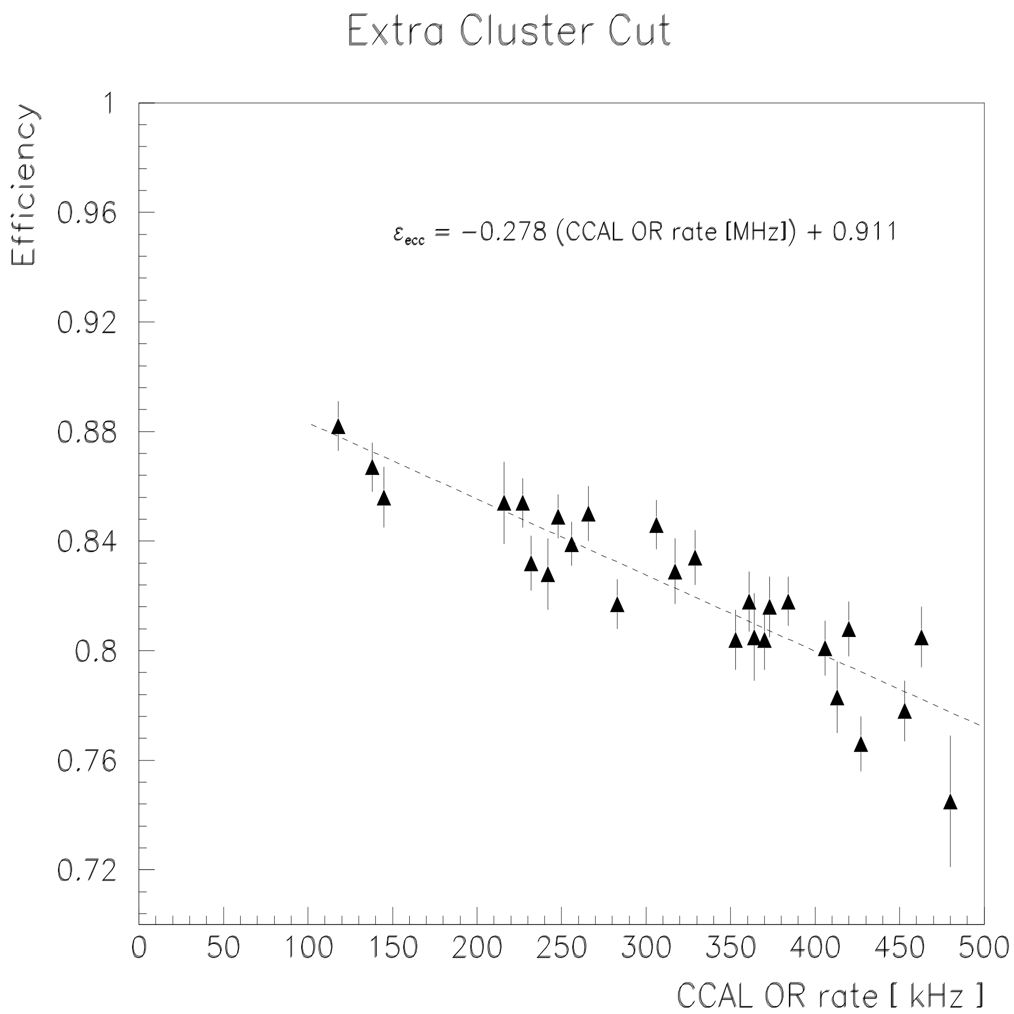

Figure 7.16: The efficiency of the extra cluster cut as a function of central calorimeter rate for $\pi^o\pi^o$ events.

of rate for good $\pi^o\pi^o$ events; a fit gives

$$\epsilon_{ecf} = (0.979 \pm 0.004) - (0.881 \pm 0.035) \times (\text{H1H2 OR rate in MHz}), \tag{7.40}$$

where the H1H2 OR[8] rate is used since the FCAL OR threshold changed in the middle of the 1991 data taking. For the 7γ analysis, the $\pi^o\pi^o$ events that have the FCAL OR bit ON are removed from the data sample and the forward calorimeter

[8]The H1H2 OR is the coincidence between the H1 OR and H2 OR.

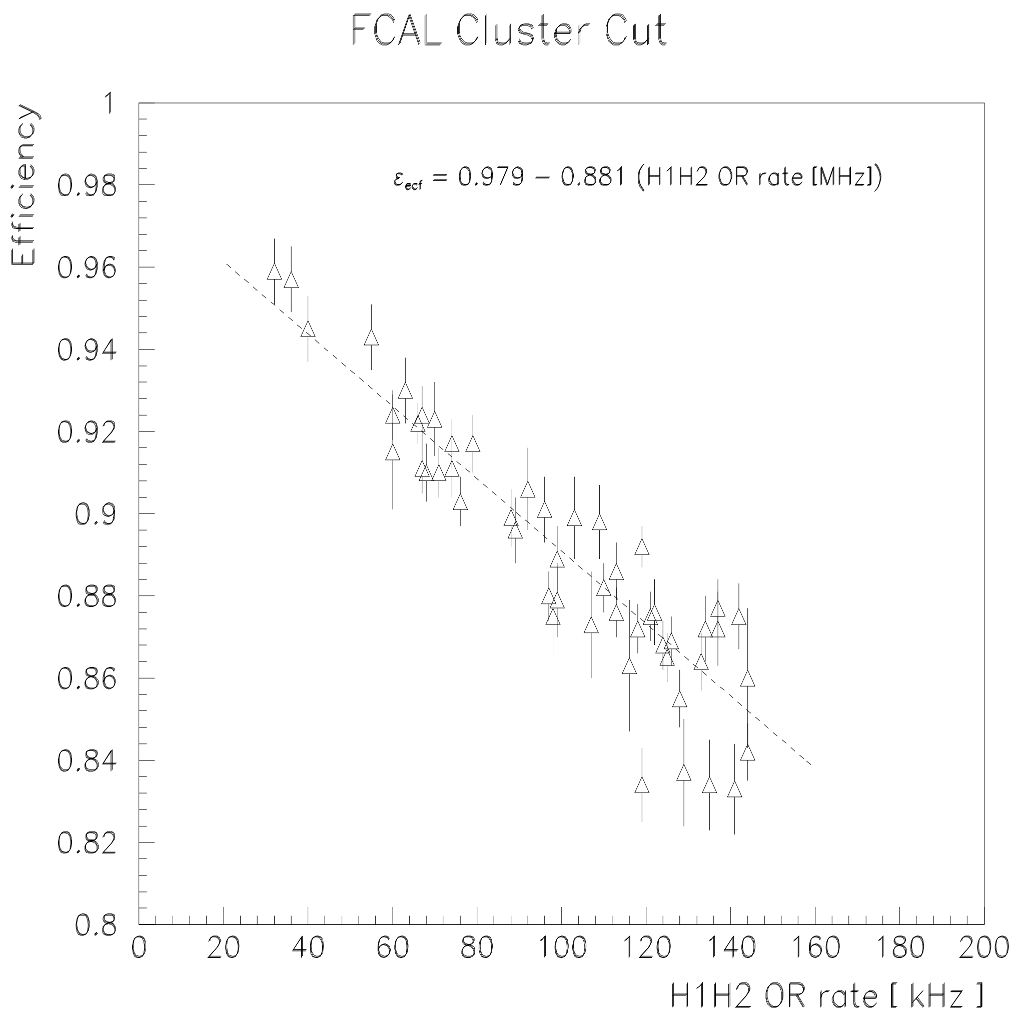

Figure 7.17: The efficiency of the forward calorimeter cluster cut as a function of H1H2 OR rate for $\pi^o\pi^o$ events.

cluster cut is found to be rate dependent,

$$\epsilon'_{ecf} = (0.993 \pm 0.004) - (0.694 \pm 0.035) \times (\text{H1H2 OR rate in MHz}), \qquad (7.41)$$

as shown in figure 7.18.

The 3γ analysis includes cuts of π^o and η particles. The efficiency of this cut is determined from the event Monte Carlo and using the cut upon the sample of the χ_2

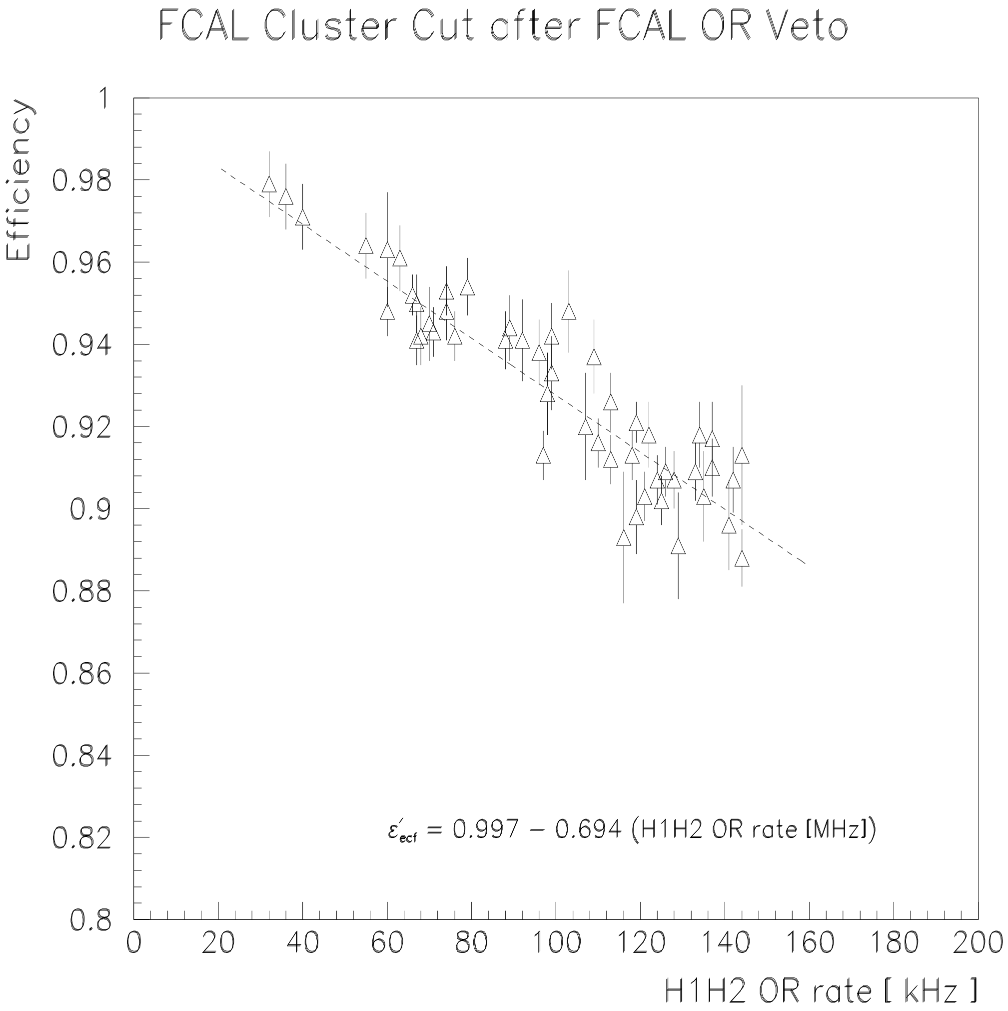

Figure 7.18: The efficiency of the forward calorimeter cluster cut as a function of H1H2 OR rate for $\pi^o\pi^o$ events; events with the FCAL OR bit ON in the trigger are removed from the sample.

events. Both results determine the π^o and η cut to be

$$\epsilon_{\pi^o\eta} = 0.81 \pm 0.01. \tag{7.42}$$

The χ^2 fit probability is required to be greater than 10%. The 3γ analysis efficiency is

$$\epsilon_{an}(3\gamma) = \epsilon_{cl}^3 \times \epsilon_{ecc} \times \epsilon_{ecf} \times \epsilon_{\pi^o\eta} \times \epsilon_{fit}; \tag{7.43}$$

Reaction $\bar{p}p \to {}^1\mathrm{P}_1 \to$	Geometrical Acceptance α_{geom}	Pile-up Cut Efficiency ϵ_{pile}	Cluster Mass Efficiency ϵ'_{cl}	Fit Analysis Efficiency ϵ_{fit}
$\gamma\eta_c \to \pi^o\pi^o\pi^o\gamma$	0.1805	0.976	0.892	0.315
$\gamma\eta_c \to \pi^o\pi^o\eta\gamma$	0.1361	0.977	0.908	0.386
$\gamma\eta_c \to \pi^o\pi^o\eta'\gamma$	0.1173	0.978	0.922	0.421
$\gamma\eta_c \to \pi^o\eta\eta\gamma$	0.0995	0.994	0.937	0.388
$\gamma\eta_c \to \pi^o\eta\eta'\gamma$	0.0862	0.987	0.932	0.415
$\gamma\eta_c \to \pi^o\eta'\eta'\gamma$	0.0820	0.987	0.916	0.450
$\gamma\eta_c \to \eta\eta\eta\gamma$	0.0738	0.998	0.944	0.425
$\gamma\eta_c \to \eta\eta\eta'\gamma$	0.0684	0.998	0.934	0.656
$\gamma\eta_c \to \eta\eta'\eta'\gamma$	0.0758	1.000	0.925	0.482
$\gamma\eta_c \to \eta'\eta'\eta'\gamma$	0.1344	1.000	0.899	0.455
$\gamma\eta' \to \pi^o\pi^o\pi^o\gamma$	0.1789	0.934	0.851	0.347
$\gamma\eta' \to \pi^o\pi^o\eta\gamma$	0.1856	0.934	0.805	0.375
$\gamma\eta \to \pi^o\pi^o\pi^o\gamma$	0.3408	0.946	0.540	0.355

Table 7.10: The Monte Carlo geometrical acceptances and the analysis efficiencies for the 7γ final states as determined from 10,000 Monte Carlo events. The cluster mass cut efficiencies for the 7γ final states are determined by whenever two gamma rays are less than 100 mrad apart.

using the average cluster cut efficiencies, $\epsilon_{an}(3\gamma) = 0.47$. The efficiency ranges from 0.42 to 0.54 and the luminosity weighted stack efficiencies range from 0.45 to 0.50.

The 7γ event Monte Carlo has been used to study the pile-up cut and the cluster mass cut efficiencies (how often two of the gamma rays are less than 150 mrad apart); these are shown for each 7γ final state in table 7.10. The 7γ analyses involve comparison to several background hypotheses; included in table 7.10, are the efficiencies for the correct hypothesis being the best fit for 10,000 Monte Carlo events. The 7γ analysis efficiency is

$$\epsilon_{an}(7\gamma) = \epsilon_{ecc} \times \epsilon'_{ecf} \times \epsilon_{pile} \times \epsilon'_{cl} \times \epsilon_{fit} \tag{7.44}$$

and is dependent upon the final state.

Reaction $\bar{p}p \to {}^1\mathrm{P}_1 \to$	Final Efficinecy		
$J/\psi\pi^o$	0.32	$\pm$	0.02
$J/\psi\pi^o\pi^o$	0.12	$\pm$	0.01
$J/\psi\pi^+\pi^-$	0.067	$\pm$	0.005
$\gamma\eta_c \to \gamma\gamma\gamma$	0.15	$\pm$	0.02
$\gamma\eta_c \to \pi^o\pi^o\pi^o\gamma$	0.029	$\pm$	0.002
$\gamma\eta_c \to \pi^o\pi^o\eta\gamma$	0.027	$\pm$	0.002
$\gamma\eta_c \to \pi^o\pi^o\eta'\gamma$	0.026	$\pm$	0.002
$\gamma\eta_c \to \pi^o\eta\eta\gamma$	0.021	$\pm$	0.002
$\gamma\eta_c \to \pi^o\eta\eta'\gamma$	0.019	$\pm$	0.001
$\gamma\eta_c \to \pi^o\eta'\eta'\gamma$	0.019	$\pm$	0.001
$\gamma\eta_c \to \eta\eta\eta\gamma$	0.017	$\pm$	0.001
$\gamma\eta_c \to \eta\eta\eta'\gamma$	0.024	$\pm$	0.002
$\gamma\eta_c \to \eta\eta'\eta'\gamma$	0.020	$\pm$	0.002
$\gamma\eta_c \to \eta'\eta'\eta'\gamma$	0.032	$\pm$	0.002
$\gamma\eta' \to \pi^o\pi^o\pi^o\gamma$	0.029	$\pm$	0.002
$\gamma\eta' \to \pi^o\pi^o\eta\gamma$	0.031	$\pm$	0.002
$\gamma\eta \to \pi^o\pi^o\pi^o\gamma$	0.036	$\pm$	0.002

Table 7.11: The final efficiencies for the different reactions.

7.5 Final Efficiencies

The final efficiency for a particular reaction is the product of the geometrical acceptance, trigger efficiency and analysis efficiency:

$$\epsilon_{tot} = \alpha_{geom} \times \epsilon_{trig} \times \epsilon_{an}. \tag{7.45}$$

The $J/\psi\pi^o$ and $J/\psi\pi^o\pi^o$ channel efficiencies are essentially not rate dependent and the total efficiency[9] is given in table 7.11. The average rates are used to calculate the final efficiency for $J/\psi\pi^+\pi^-$ (3γ) that is presented in table 7.11; the range of efficiencies is 0.057 to 0.079 (0.13 to 0.18). The 7γ final efficiencies are also presented

[9]For $J/\psi\ \pi^o$, the median value for the range of α_{geom} in table 7.3 is used.

in table 7.11 using the average rates; the efficiencies range around the values in the table by $\pm 15\%$.

Data from the ψ' resonance confirms the efficiency determination for the $J/\psi\pi\pi$ channels. The expected number of events ($\psi' \to J/\psi\pi^o\pi^o, J/\psi\pi^+\pi^-$) is determined from the observed number of $\psi' \to e^+e^-$ and corrected for acceptances, efficiencies and branching fractions [21]. The expected number of events for $J/\psi\pi^o\pi^o$ ($J/\psi\pi^+\pi^-$) is 122 ± 6 (109 ± 10); the observed number is 113 (104).

7.6 Energy and Luminosity Uncertainties

The beam center of mass energy is

$$E_{cm}^2 = 2(1+\gamma)(m_p c^2)^2; \tag{7.46}$$

the uncertainty of the center of mass energy for any data run is

$$\delta E_{cm} = \frac{\gamma^3 m_p^2 c^4 \beta^2}{E_{cm}} \frac{\delta\beta}{\beta}. \tag{7.47}$$

The velocity uncertainty is from equation 2.2 and is

$$\frac{\delta\beta}{\beta} = \sqrt{\left(\frac{\delta f}{f}\right)^2 + \left(\frac{\delta L}{L}\right)^2}, \tag{7.48}$$

where the length uncertainty is $\delta L = \delta L_0 + \delta(\Delta L)$. The frequency measurement is made accurately, $\frac{\delta f}{f} = 1.5 \times 10^{-7}$. The reference orbit length uncertainty is due to the mass uncertainty of the ψ'; the reference orbit length is 474.048 m with an uncertainty of 0.67 mm which corresponds to the ψ' mass uncertainty of 0.1 MeV/c^2 [21]. The deviation of the orbit length measured by the BPMs has an estimated uncertainty of 1 mm due to the least significant bit of the BPMs. The overall uncertainty of the beam energy is 190 keV.

The uncertainty in the luminosity monitor's determination of the luminosity is dependent upon the uncertainties of the $\bar{p}p$ elastic cross section in this region (2.0%) and the geometrical acceptance of the silicon detector (2.0%). These combine for a systematic error of 4.0%. A statistical error of 3% for the luminosity determination comes from the necessity to subtract an exponential background from the pulse height spectrum, see figure 2.7.